Applied Ocean Research 129 (2022) 103388

Contents lists available at ScienceDirect

Applied Ocean Research

journal homepage: www.elsevier.com/locate/apor

Peak uplift resistance of offshore slender structures shallowly buried in the sloping seabed considering wave actions

Hongkuan Yang [a], Zhen Guo [a,b,*], Lizhong Wang [a], Wengang Qi [c]

[a] Key Laboratory of Offshore Geotechnics and Material of Zhejiang Province, College of Civil Engineering and Architecture, Zhejiang University, Hangzhou 310058, China
[b] Hainan Institute of Zhejiang University, Sanya 572000, China
[c] Key Laboratory for Mechanics in Fluid Solid Coupling Systems, Institute of Mechanics, Chinese Academy of Sciences, Beijing 100190, China

ARTICLE INFO

Keywords:
Sloping seabed
Wave actions
Slender structures
Peak uplift resistance
Reduction

ABSTRACT

The current practice for the pipe-soil interaction mainly focuses on the pipelines which are buried in the level ground, and ocean waves are rarely considered. However, sloping topographies and wave actions are often encountered by offshore slender structures. This study numerically investigated their peak uplift resistances, taking multiple factors, i.e., the slope effect and wave effect, into account simultaneously. The numerical model was first verified by the available analytical and experimental results. It was found that the normalized peak uplift resistance decreases as the slope angle increases, especially for smaller burial ratios. The presence of wave troughs weakens the traditional peak uplift resistance. For the given burial ratio and slope angle, the reduction in the peak uplift resistance increases almost linearly with the local wave steepness. For steeper slopes and smaller burial ratios, this reduction becomes larger because of more intense upward seepage. The effects of local relative water depth and wave period were also studied. Finally, a preliminary formula for the reduction in the peak uplift resistance of shallowly-buried offshore slender structures was proposed to consider the slope effect and wave effect.

1. Introduction

Slender structures are wildly applied in the ocean engineering. Mooring lines, umbilicals, risers and pipelines are prevalent in the offshore oil and gas industry as hydrocarbons continue to be extracted. Bottom-mounted slender structures, such as monopile foundations, are also extensively used to install the growing number of offshore wind farms over the decades, accompanied with another application of slender structures, submarine power cables. Moreover, there are submarine communication cables constructed on the seabed to transmit digital data between land-based stations. And Carter et al. (2009) reported that the total length of submarine communication cables in the world's oceans has exceeded one million kilometers.

Slender structures in the offshore environment, especially the focus of this study, submarine pipelines and cables, are generally buried in the seabed to provide protection from anchors and fishing gear, to provide thermal insulation, and to mitigate the risks of pipeline upheaval buckling (Haigh, 2021). Among them, the upward stability of slender structures has been investigated by many scholars (Trautmann et al., 1985; White et al., 2008, 2011; Jung et al., 2013; Roy et al., 2018a, 2018b; Robert and Thusyanthan, 2018). Ismail et al. (2021) summarized classical predictive analytical models for the pipeline uplift resistance. In industry, there are some widely-used codes developed for the pipeline uplift resistance, such as American Lifelines Alliance (ALA, 2005) and Det Norske Veritas (Det Norske Veritas DNV, 2007), and these codes are also available for the cable design. The current design guidelines generally assume that structures are buried in the level ground. However, rugged terrains are often encountered by the routes of submarine slender structures. For the sloping seabed, Gao et al. (2012, 2016) investigated the upslope/downslope lateral soil resistance of the untrenched pipelines undertaken the hydrodynamic load. The significance of the slope angle on these lateral resistances was substantiated. Katebi et al. (2021) showed full-scale experimental results and extended numerical simulations for the lateral force-displacement response of the buried pipelines in slopes. It was found that the soil force on the pipeline rises with increase in the slope grade and burial depth ratio. More less attention was paid in the past to the upward movement of the slender structures buried in slopes. The uplift of the pipelines buried in the sloping medium dense sand was experimentally studied in Huang et al. (2021a), and a reduction in the peak uplift resistance with increasing the slope angle (up to 10% reduction for 20° slope) was observed.

* Corresponding author.
E-mail address: nehzoug@163.com (Z. Guo).

https://doi.org/10.1016/j.apor.2022.103388
Received 31 August 2022; Received in revised form 27 September 2022; Accepted 17 October 2022
Available online 26 October 2022

Nomenclature

a (=43.75(1-exp(−19m)))	a function of the seabed slope
b (=1.56/(1+exp(−19.5m)))	another function of the seabed slope
c	wave phase velocity
D	structure outer diameter
d	local water depth
d_i	water depth of the incident wave
d_p	local water depth corresponding to the burial location
E	wave energy density
E_p	Young's modulus of the structure
E_s	Young's modulus of soil
f	uplift resistance factor in DNV (2007)
F_p	peak uplift resistance
$f_{s,w}$	normalized peak uplift resistance considering both the slope effect and wave effect
$f_{s0,w0}$	normalized peak uplift resistance for the level seabed and without wave action
g (=9.81m/s^2)	gravity acceleration
H	local wave height
h	local seabed thickness
H_c	burial depth (the vertical distance from the structure center to the seabed surface)
H_i	incident wave height
H_p	local wave height corresponding to the burial location
H_t (=H_c-0.5D)	vertical distance from the ground surface to the pipeline crown
j'_c	opposite normalized vertical average gradient of the excess pore pressure at the depth H_c with respect to that at the seabed surface
k (=2π/L)	wave number
L	local wave length
L_p	local wave length corresponding to the burial location
m (=tanα)	seabed slope
n	rate of the wave energy transfer
p_c	wave-induced excess pore pressure at the depth H_c
p_w	hydrodynamic pressure at the seabed surface
$\lvert p_w \rvert$	amplitude of the hydrodynamic pressure on the seabed surface
r	roughness parameter in DNV (2007)
R	reduction in the peak uplift resistance due to the slope effect and wave effect
R_{max}	the maximum uplift resistance recommended by DNV (2007)
R_s	reduction in the peak uplift resistance due to the slope effect
R_w	reduction in the peak uplift resistance due to the wave effect
T	incident wave period
t	time
t_w	wall thickness of the structure
u_e	excess pore pressure
$\lvert u_e \rvert$	amplitude of the excess pore pressure
W_p'	effective weight of the structure
x	horizontal coordinate
z	vertical coordinate
α	slope angle
γ'	effective unit weight of soil
γ_w (=9810N/m^3)	unit weight of water
$\Delta\sigma'_{xx}$	variation of the horizontal effective stress
$\Delta\sigma'_{zz}$	variation of the vertical effective stress
$\Delta\tau'_{xz}$	variation of the shear stress in the x-z plane
μ	interface friction coefficient of the structure outer surface
ν_p	Poisson's ratio of the structure
ν_s	Poisson's ratio of soil
σ'	normal effective stress
σ'_{xx}	horizontal effective stress
σ'_{zz}	vertical effective stress
τ	shear stress
τ_{xz} (=τ_{zx})	shear stress in the x-z plane
φ	friction angle of soil
ψ	dilation angle of soil
ω (=2π/T)	wave angular frequency

The upward motion of slender structures may be induced by wave actions, especially during storms. For instance, Herbich et al. (1984) reported that a pipeline with a diameter of 3.05 m was found to float up to the bed surface after an extreme storm in the construction period. Similar phenomenon may be due to the seabed liquefaction, because the seabed may suffer the momentary liquefaction (Zen and Yamazaki, 1990, 1991; Hsu and Jeng, 1994; Liang et al., 2020; Hsu et al., 2021;) or the residual liquefaction (Sumer et al., 1999; Sassa and Sekiguchi, 1999, 2001; Teh et al., 2003; Miyamoto et al., 2004, 2020; Dunn et al., 2006; Jeng and Zhao, 2015; Ülker, 2021) under wave actions. The sinking or floatation of a slender structure in a liquefied seabed depends on the structure specific gravity and liquefied soil parameters (Sumer et al., 1999; Teh et al., 2003; Damgaard et al., 2006; Sumer et al., 2006; Det Norske Veritas DNV, 2017). However, the uplift of the structures buried in the unliquefied seabed also deserves special attention, considering that (1) waves may induce upward force on a buried structure (Cheng and Liu, 1986; Sudhan et al., 2002; Roopsekhar and Sundar, 2004; Magda et al., 2000; Neelamani and Al-Banaa, 2012), although the uplift may also be induced by anchors and fishing gear, or the thermal buckling for pipelines; and (2) the strength of the overburden soil may be weakened by waves (Magda et al., 2000; Bonjean et al., 2008; Chen et al., 2019; Qi et al., 2020). It is risky to ignore the wave effect when accessing the peak uplift resistance of a slender structure. The aforementioned strength reduction may result from either the build-up of the residual excess pore pressure or the transient upward seepage under the wave trough. This study is limited to the latter, and in this regard, Qi et al. (2020) developed a poro-elastoplastic model to investigate the uplift soil resistance to a shallowly-buried pipeline in the sandy seabed under waves. The peak vertical soil resistance of the buried pipeline indeed decreases after the wave load applied. A resistance reduction coefficient was introduced to characterize the wave effect and it was found that this coefficient decreases linearly with the normalized amplitude of the wave pressure at the seabed mudline. However, the pipeline was buried in a level seabed, and both the burial depth ratio and outer pipeline diameter were constant in their study. More complex situations encountered in practice still need to be further studied.

In order to investigate the uplift resistance of the offshore slender structures shallowly buried in slopes under wave actions, this study considers multiple factors that were usually neglected in the previous practice, i.e., the slope effect and wave effect. The numerical model is introduced at first and verified by the available analytical/experimental results subsequently. The slope effect and wave effect on the peak uplift resistance are then studied considering various slope angles, burial ratios, and waves of different parameters. Finally a preliminary predictive formula for the reduction in the peak uplift resistance is proposed.

2. Numerical methodology

Fig. 1 gives the layout of this two-dimensional numerical simulation. For the purpose of description, a Cartesian system is established. The

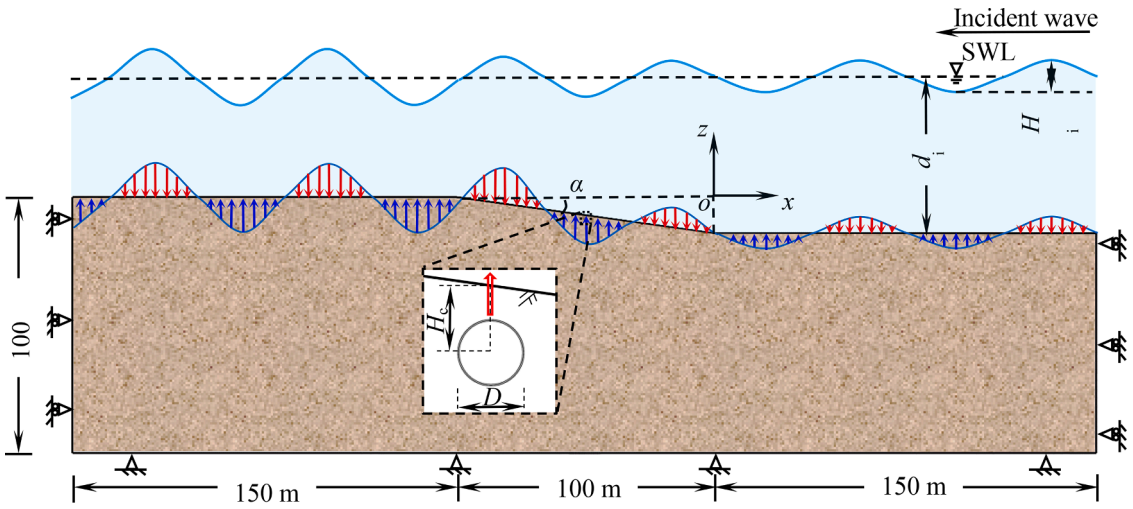

Fig. 1. Layout of the numerical model uplifting the circular structure buried in sloping seabed considering wave actions.

incident wave with the water depth d_i, height H_i and period T propagates from the deep water, climbs along the sloping seabed and reaches the shallow water. Note that the subscript i in this study implies the incident quantities. And this process is accompanied with the hydrodynamic pressure variation on the seabed surface. The sloping seabed with the slope angle α, length 100 m is located between two level seabeds of length 150 m. And the maximum thickness of the seabed is 100 m. A slender structure (pipeline or cable), with the circular section of outer diameter D, is buried at $x = -50$ m, the middle of the sloping seabed. The burial depth H_c represents the vertical distance from the structure center to the seabed surface. The commercial software Abaqus/Standard was used to carry out this numerical simulation.

Similar to Gatmiri (1990), Ulker et al. (2009), and Rafiei et al. (2019), the linearly shoaling theory is adopted to describe the wave transformation on the slope. It assumes that the wave energy is conserved and the wave period is constant during the whole process, that is, for any propagation profile 1 and 2, there is always:

$$(Ecn)_1 = (Ecn)_2 \tag{1}$$

where the wave energy density E and its propagation velocity (cn) are given below:

$$E = \frac{\gamma_w H^2}{8} \tag{2}$$

$$cn = \frac{1}{2}c\left(1 + \frac{2kd}{\sinh 2kd}\right) \tag{3}$$

in which γ_w (=9810 N/m^3) is the unit weight of the water; H is the local wave height; c is the phase velocity; d is the local water depth; and $k = 2\pi/L$ and L is the local wave length that can be solved through the dispersion relation:

$$L = \frac{gT^2}{2\pi}\tanh kd \tag{4}$$

where g (=9.81 m/s^2) is the gravity acceleration. After the local wave parameters solved from Eqs. (1)–(4), hydrodynamic pressure p_w is applied to the seabed surface using the user-defined subroutine DLOAD (A user subroutine to prescribe distributed loadings. It is also used to apply concentrated or distributed wind, wave, or buoyancy loading in an Abaqus/Aqua analysis.) according to the linear theory:

$$p_w = \frac{\gamma_w H}{2\cosh kd}\cos(kx + \omega t) \tag{5}$$

in which the angular frequency $\omega = 2\pi/T$ and t is the time. Various incident wave conditions are considered in this study and they are summarized in Table 1. In the present study, only unbroken waves are studied, and the following breaking wave steepness $(H/L)_b$ in Miche (1944) for the horizontal bathymetry is considered:

$$\left(\frac{H}{L}\right)_b = \frac{1}{7}\tanh\left(2\pi\frac{d}{L}\right) \tag{6}$$

Meanwhile, for the breaking wave height on the sloping seabed, the most widely used empirical formula is adopted, in terms of the ratio of breaking wave height to water depth, $(H/d)_b$, derived by Weggel (1972) using data from a large number of experiments:

$$\left(\frac{H}{d}\right)_b = \frac{b}{1 + \frac{ad}{gT^2}} \tag{7}$$

where a and b are functions of the seabed slope, m, given by $a = 43.75(1\text{-}\exp(-19\,m))$ and $b = 1.56/(1+\exp(-19.5\,m))$. In addition, the incident wave with $d_i = 42$ m, $H_i = 9.5$ m and $T = 7$ s has the longest wave length of $L_i = 76.35$ m, roughly equal to the half of the length of the level seabed. Hence the boundary effect on the both sides could be eliminated (Ye and Jeng, 2012). What is more, the seabed approaches to be of infinite depth since L_i<local seabed thickness h (Hsu and Jeng, 1994).

Since the wave-induced excess pore pressure response is the key of the considered problem, soils module is employed to solve for the

Table 1
Parameters for this numerical model uplifting circular structure buried in sloping seabed considering wave actions.

Wave parameters	
Water depth d (m)	33.0, 36.0, 39.0, 42.0
Wave height H (m)	1.0, 3.5, 6.5, 9.5
Wave period T (s)	5.5, 6.0, 6.5, 7.0
Seabed parameters	
Slope angle α (°)	0, 2, 4, 6, 8
Effect unit weight γ'(kN/m^3)	11.674
Young's modulus E_s (kPa)	4047
Poisson's ratio ν_s	0.33
Friction angle φ (°)	35
Dilation angle ψ (°)	5
Structure parameters	
Burial ratio H_c/D	1.0, 1.5, 2.0, 2.5, 3.0
Effective weight W_p' (N/m)	3425.95
Outer diameter D (m)	1.0
Wall thickness t_w (mm)	20
Young's modulus E_p (GPa)	204
Poisson's ratio ν_p	0.3
Interface friction coefficient μ	0.32

transient excess pore pressure. In Qi et al. (2020), elaborated assumptions and theories about this module was illustrated, and only key points are shown here:

(1) The inertia effect can be ignored when solving the wave-induced seabed response, and the seepage flow within the seabed is assumed to obey Darcy's law.
(2) This study aims at saturated sandy seabed, so that for the steady-state coupled pore fluid diffusion and stress analysis, original continuity equation degrades into the following Laplace's equation:

$$\nabla^2 p = 0 \tag{8}$$

The classical elastoplastic Mohr-Coulomb model has been widely used by geotechnical engineers to model the sand-pipeline interaction because of its practicability (Roy, 2012; Kouretzis et al., 2013; Chaloulos et al., 2015; Katebi et al., 2021), and it has been verified that this model captures the peak soil resistance well, although the mobilized displacement and post-peak softening are not well simulated. However, this study primarily focuses on the peak uplift resistance of the structure. Thus, not considering the wave-induced excess pore pressure accumulation, for the offshore sloping seabed composed of medium dense sand, this constitutive model is adopted again. The seabed parameters are listed in Table 1. Note that the submarine slope angles α listed are less than 10°, which is a common phenomenon in nature.

The circular structure is modeled with the elastic material and it is shallowly buried at different depths. All structure parameters are given in Table 1. The interface between the outer surface and the surrounding soil is defined as "hard" contact in normal behavior while a Coulomb friction model with the friction coefficient μ of 0.32 (=tan(φ/2)) is used in tangential behavior.

The 4-node bilinear plane strain quadrilateral element (CPE4) and 4-node plane strain quadrilateral, bilinear displacement, bilinear pore pressure element (CPE4P) are used to simulate the structure and the seabed soil, respectively. As shown in Fig. 2, structured meshes are generated in the computational domain. The structure periphery is divided into 48 uniform segments, and the structure is surrounded by a parallelogram of 2D in the vertical direction, within which the radial lines are divided into 6 uniform segments. The meshes around the structure are refined within the width of 5.5D width that is much larger than the maximum influence area when the structure is uplifted (Abduljauwad et al., 2004). The elements within this region have a size of D/6 in the vertical and horizontal directions, while the size of the elements outside this region is 3.35D in the horizontal direction. In addition, all vertical sizes of the elements below the aforementioned parallelogram are 1.55D. Other sizes can be determined according to the structured rules. Boundary conditions are indicated in Fig. 1. On the two lateral sides, the normal displacement is not allowable while the bottom is fully fixed, and no displacement constraints are applied to the seabed surface. With regard to the hydraulic boundary conditions, the user-defined subroutine DISP (A user subroutine to specify prescribed boundary conditions in Abaqus) must be used to satisfy the condition excess pore pressure u_e=p_w on the seabed surface, so that the vertical effective stress there vanishes. All rest surfaces including the structure surface are considered to be impermeable.

The implementation of this numerical model is as follows. (1) Considering the gravity, the geo-stress equilibrium was reached at the first step. (2) The hydrodynamic pressure on the seabed surface is applied according to the aforementioned wave theory, and the steady excess pore pressure field is formed within the seabed soil. Note that the structure lies just below the local wave trough. (3) The structure is uplifted under the displacement-controlled loading, and the peak resistance is read off from the force-displacement curve.

3. Verification of the numerical model

To the authors' knowledge, no laboratory experiments are available on the uplift resistance of the offshore pipelines/cables shallowly buried in the sloping seabed and with wave actions considered. Thus the developed numerical model is validated by three parts: (1) wave-induced seabed response, (2) peak uplift resistance of the structure buried in the level ground, and (3) peak uplift resistance of the structure buried in the sloping ground.

Madsen (1978) developed a general theory for the excess pore pressure and effective stress induced in the porous seabed by ocean waves. For saturated and elastic isotropic seabed of infinite depth, the analytical solution can be expressed in terms of the variation of horizontal effective stress$\Delta\sigma'_{xx}$, vertical effective stress$\Delta\sigma'_{zz}$, shear stress$\Delta\tau'_{xz}$ and excess pore pressure u_e:

$$\Delta\sigma'_{xx} = -\Delta\sigma'_{zz} = \frac{\gamma_w H}{2\cosh kd} kze^{kz}\cos(kx+\omega t) \tag{9a}$$

$$\Delta\tau'_{xz} = \frac{\gamma_w H}{2\cosh kd} kze^{kz}\sin(kx+\omega t) \tag{9b}$$

$$u_e = \frac{\gamma_w H}{2\cosh kd} e^{kz}\cos(kx+\omega t) \tag{9c}$$

The response of a level seabed undertaken the linear wave action is numerically investigated in this study, with the wave and seabed parameters listed in Table 2. Note that it is found that there is no plastic deformation of the seabed after applying the predefined hydrodynamic pressure. Both the numerical result and analytical solution in Madsen (1978) are plotted in Fig. 3. All response results are normalized by the amplitude of the hydrodynamic pressure on the seabed surface $|p_w|$. It can be seen that the results are in good agreement.

Trautmann et al. (1985) experimentally investigated the uplift force-displacement response of buried pipelines, in which the influence of soil density and burial depth were taken into account. Results of their tests in medium and dense sand are employed to verify this numerical model. Both the soil and pipeline parameters, previously determined by Roy (2012), are given in Table 3. And Fig. 4 shows the normalized peak uplift resistance $F_p/\gamma' H_c D$ for different burial depth ratios H_c/D. Both numerical and experimental $F_p/\gamma' H_c D$ increases with increasing H_c/D in

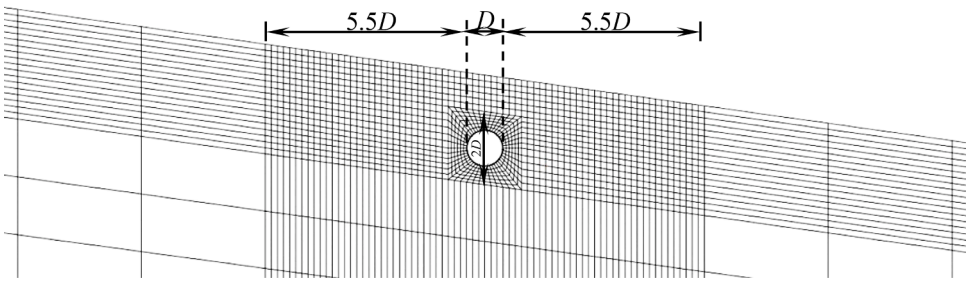

Fig. 2. Mesh distribution around the structure.

Table 2
Parameters for the analytical solutions in Madsen (1978).

Wave parameters	
Water depth d (m)	4.0
Wave height H (m)	2.0
Wave period T (s)	7.0
Wave length L (m)	41.4
Seabed parameters	
Seabed thickness h (m)	42.0
Effect unit weight γ'(kN/m^3)	11.674
Young's modulus E_s (kPa)	26,600
Poisson's ratio ν_s	0.33
Friction angle φ (°)	44
Dilation angle ψ (°)	16

medium and dense sand, respectively. And the results of the simulation are in reasonable accordance with those recorded in the experiments, implying the applicability of the numerical model in the uplift resistance of the pipeline buried in the level ground.

Huang et al. (2021a) performed a series of 30-g centrifuge experiments to study the uplift behavior of the buried pipeline in medium dense sand with the slope angles α of 0°, 10°, 20°, and various burial depths. Cases of I−2, II−2 and III−2 are used to verify the developed numerical model, in which the pipeline were buried at depth H_t=2D (H_t=H_c-0.5D, the vertical distance from the ground surface to the pipeline crown). The soil and pipeline parameters can be determined from Huang et al. (2021b) and they are shown in Table 4. Note that the elastic parameters of the soil were not reported by Huang et al., and they are set to be the same values as those in this study, i.e., representative properties of the medium dense sand, considering that these parameters were found to have little effect on the peak uplift resistance Qi et al. (2020). In addition, the pipeline used in their experiment has a smooth surface, thus no interface friction coefficient is listed. Fig. 5 gives the normalized peak uplift resistance $F_p/\gamma' H_t D$ against the slope angle α. The numerical results generally match the experimental ones and a reduction in the peak resistance is observed when increasing the slope angle. However, it can be found that the numerical results are a little larger than the experimental ones for any slopes. It is supposed that this overestimation may be attributed to the inaccurate determination of the internal friction angle φ or dilation angle ψ, or their constant nature in Mohr-Coulomb model. Overall, the developed numerical model could reasonably capture the peak uplift resistance of the pipeline buried in the sloping ground.

In summary, the numerical model could well solve the wave-induced seabed response and capture reasonable peak uplift resistance of the structure buried in the level/sloping ground.

Table 3
Parameters used in the experiments by Trautmann et al. (1985).

Soil parameters	Medium state	Dense state
Effective unit weight γ'(kN/m^3)	16.4	17.7
Young's modulus E_s (kPa)	2950	3650
Poisson's ratio ν_s	0.2	0.2
Friction angle φ (°)	35	44
Dilation angle ψ (°)	5	16
Pipeline parameters		
Effective weight W_p' (N/m)	147.95	
Outer diameter D (m)	0.102	
Wall thickness t_w (mm)	6.4	
Young's modulus E_p (GPa)	204	
Poisson's ratio ν_p	0.3	
Interface friction coefficient μ	0.32	

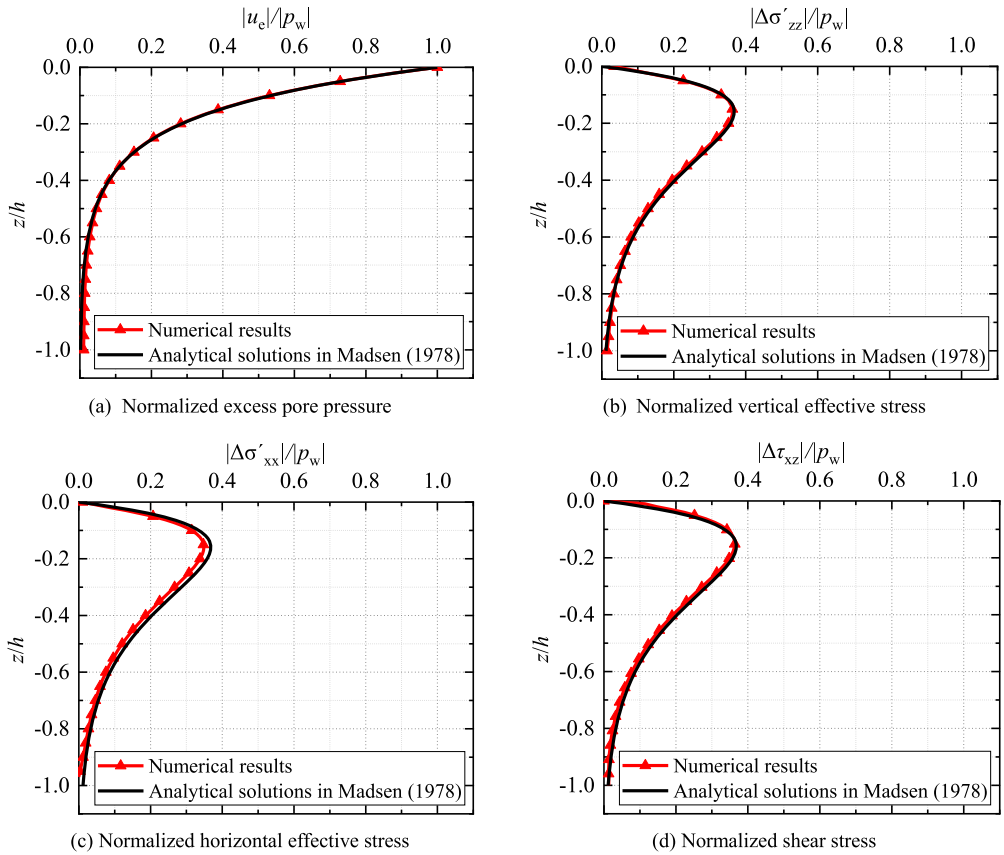

(a) Normalized excess pore pressure
(b) Normalized vertical effective stress
(c) Normalized horizontal effective stress
(d) Normalized shear stress

Fig. 3. Distribution of the normalized wave-induced (a) excess pore pressure, (b) vertical effective stress, (c) horizontal effective stress and (d) shear stress along depth.

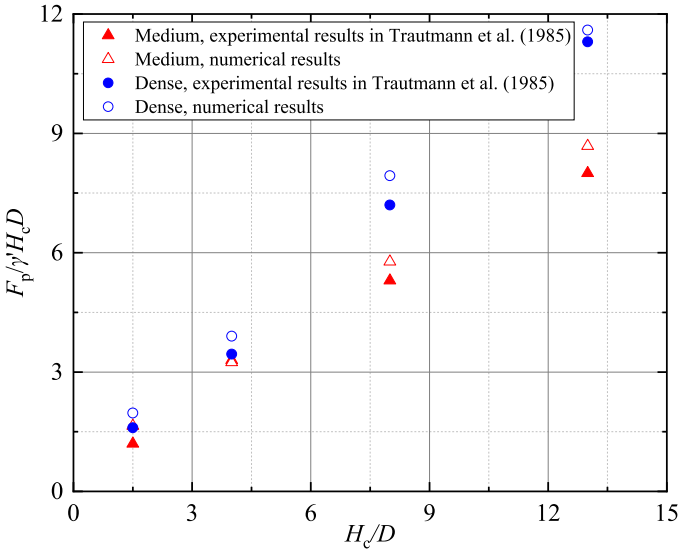

Fig. 4. Variation of the normalized peak uplift resistance with the burial depth ratio.

Table 4
Parameters (in prototype) used in centrifuge experiments by Huang et al. (2021a).

Soil parameters	
Effective unit weight γ'(kN/m^3)	14.833 at $\alpha = 0°$, 14.862 at $\alpha = 10°$, 14.891 at $\alpha = 20°$
Young's modulus E_s (kPa)	4047
Poisson's ratio ν_s	0.33
Friction angle φ (°)	41.77
Dilation angle ψ (°)	7
Pipeline parameters	
Effective weight W_p' (N/m)	5688.77
Outer diameter D (m)	1.2
Wall thickness t_w (mm)	60.0
Young's modulus E_p (GPa)	68.9
Poisson's ratio ν_p	0.33

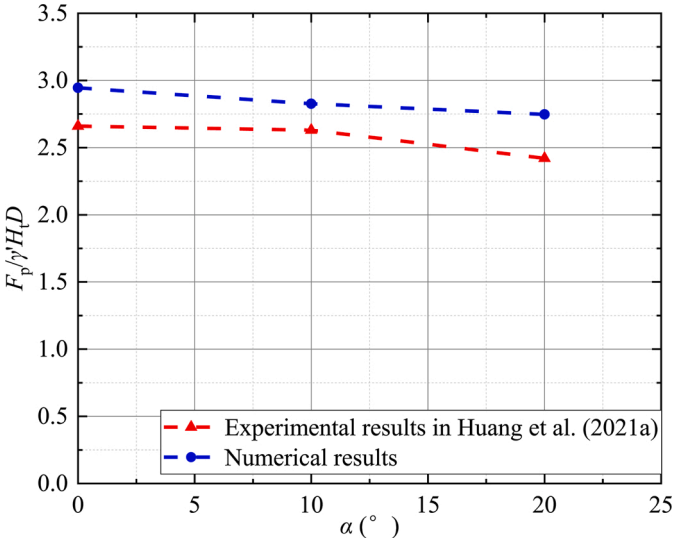

Fig. 5. Normalized peak uplift resistance against slope angle.

4. Results and analysis

The slope effect and wave effect on the peak uplift resistance are explored successively. The Section 4.1 investigates the slope effect on the peak uplift resistance of the structure buried at different depths. In the Section 4.2, the wave load is applied to the seabed surface and the combined effects of slope and wave on the peak uplift resistance are emphasized. Finally the Section 4.3 presents a preliminary predictive formula on the reduction in the peak resistance considering the slope effect and wave effect.

4.1. Effect of slope

Fig. 6(a) shows the normalized peak uplift resistance $F_p/\gamma' H_c D$ against the slope angle α for different burial ratios. It is obvious that $F_p/\gamma' H_c D$ increases with increasing the burial ratio H_c/D. More importantly, similar to Huang et al. (2021a), $F_p/\gamma' H_c D$ decreases as α increases, especially for smaller burial ratios. For the level ground, Det Norske Veritas DNV (2007) suggests that the maximum uplift resistance R_{max} of a pipe in sand can be expressed as:

$$R_{max} = \left(1 + f\frac{H_c}{D}\right)(\gamma' H_c D) \tag{10}$$

where f is the uplift resistance factor, and for pipes in medium and dense sand, a model based on the passive earth pressure theory provides the best fit to test data and:

$$f = \frac{\tan\varphi}{\left(\sqrt{1+\tan^2\varphi} - \tan\varphi\sqrt{1+r}\right)^2} \tag{11}$$

in which r is a roughness parameter and possibly near –1 for the current application. Fig. 6(b) gives the comparison between numerical results and those from Det Norske Veritas DNV (2007) using R_{max}. It is found that the latter are in fairly agreement with the numerical simulation, however, it slightly underestimates the resistance for larger burial ratios.

The shear bands at the peak uplift resistance are plotted in Fig. 7 for different slopes with $H_c/D = 1.0$. There are two main inclined and symmetrical shear bands emanating from the both sides of the structure buried in the level seabed. And these two shear bands do not extend to the seabed surfaces. However, at $\alpha > 0°$, the two main shear bands become asymmetric. Generally speaking, these two shear bands have a little rotation towards the slope toe, which is also a primary finding in Huang et al. (2021a). And the shear band near the slope crest gets wider and longer, which even propagates to the seabed surface, while the other one near the slope toe becomes narrower and shorter. Moreover, a third plastic zone near the lower left side of the structure gradually appears as the slope angle α increases. That is, compared with the level seabed, when uplifting the structure buried in slopes, more surrounding soil near the slope crest yields, but less surrounding soil near the slope toe does.

Fig. 8 gives the effective stress path, initial and maximum Mohr's circle as well as the strength line for the centroids of two representative elements at $\alpha = 0°$ and 8°. The effective stress components (σ'_{xx}, τ_{xz}) and (σ'_{zz}, τ_{zx}) of these points are also marked in these figures. Elements E_1 and E_2 are shown in Fig. 8(a): one near the upslope springline of the structure while the other near the downslope springline. Note that the effective stress path in this study is defined as the set of points of the maximum shear stress for each Mohr's circle. Corresponding results in the element E_2 at $\alpha = 0°$ are omitted due to symmetry. Notice that the difference among the initial effective stress states in Fig. 8(b–d) is not so prominent because the maximum slope angle $\alpha = 8°$ However, it is interesting to find that the change in the effective stress state in the element E_1 at $\alpha = 0°$ (Fig. 8(b)) is similar to that in the element E_1 at $\alpha = 8°$ (Fig. 8(c)), but not for the element E_2 at $\alpha = 8°$ (Fig. 8(d)). In the element E_1 at $\alpha = 0°$ and 8°, the horizontal effective stress σ'_{xx} and shear stress τ_{xz} increase when uplifting the structure, while the vertical

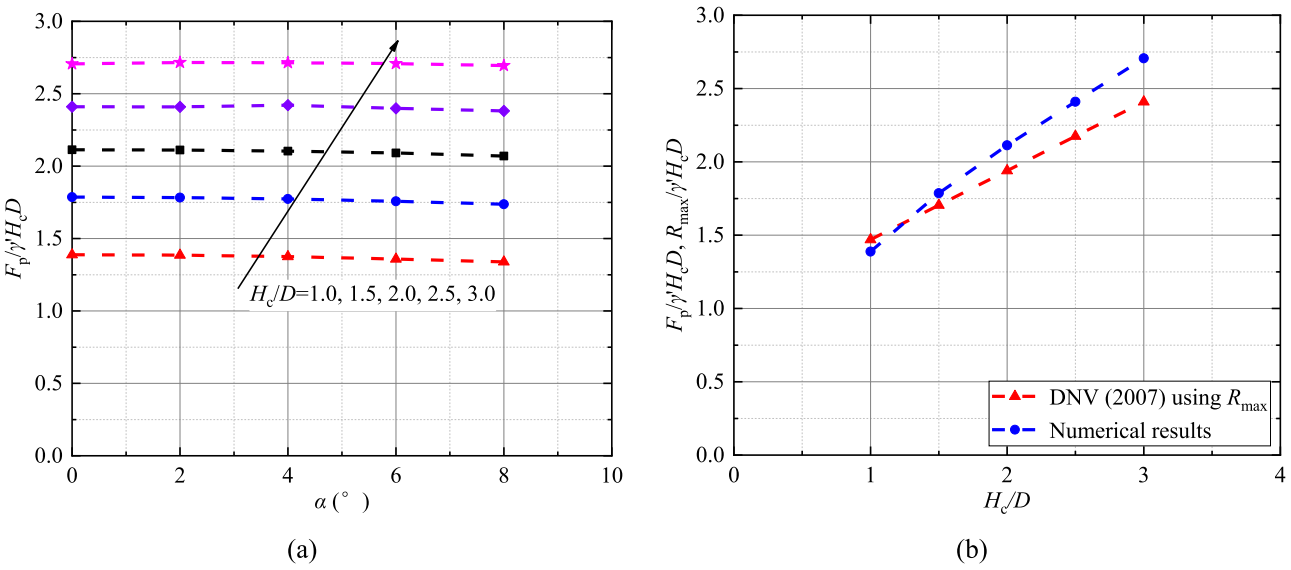

Fig. 6. (a) Effect of slope angle on the normalized peak resistance when there are no waves and (b) comparison with Det Norske Veritas DNV (2007) using R_{max} for the level seabed.

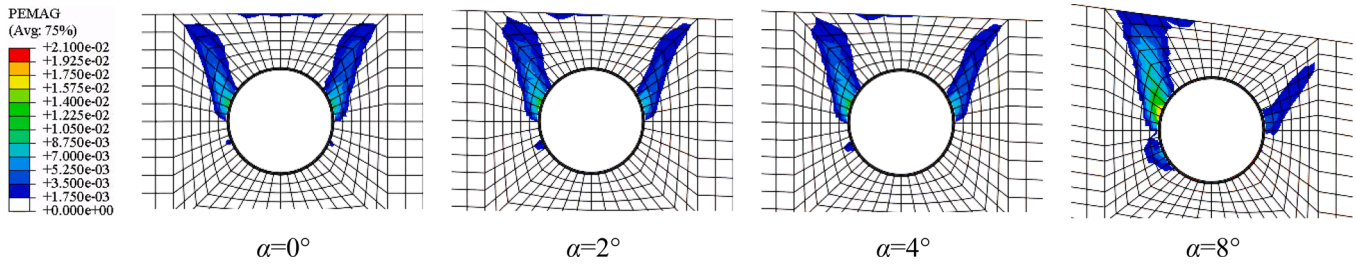

Fig. 7. Plastic strain contour at the peak uplift resistance for different slope angles (H_c/D = 1.0).

effective stress σ'_{zz} decreases until the maximum Mohr's circle is tangent to the strength line. In the element E_2 at $\alpha = 8°$, what differs from the previous two cases is that the horizontal effective stress σ'_{xx} decreases a little before the maximum Mohr's circle becomes tangent to the strength line. And the expansion of the Mohr's circle is much smaller than that in the level ground. It implies that the slope effect produces asymmetric changes in the stress state on the both sides of the structure when it is uplifted, and the reduction in the peak resistance may be caused by the lower strength mobilization of the surrounding soil near the slope toe.

4.2. Effect of wave

4.2.1. Effect of wave height

The wave load induces inhomogeneous excess pore pressure distribution within the seabed, from whose gradient, the pore fluid velocity (FLVEL, an output variable in Abaqus that represents the pore fluid effective velocity vector within the soil) is generated according to Darcy's law. And the larger this velocity is, the stonger its drag effect on the soil particles, i.e., the variation of the effective stress, becomes. Fig. 9 (b–e) shows the steady FLVEL distribution around the structure before uplift, and the distribution for the same region without structure is also plotted in Fig. 9(a). It can be seen that when there is no structure buried, the FLVEL distribution is generally homogeneous and its primary direction is upward. However, the burial of the structure disturbs the aforementioned homogeneity, making the FLVEL surrounding the structure, especially on its both sides, larger than those within the pure seabed. Moreover, the FLVEL magnitude gradually reduces as the incident wave height decreases (see Fig. 9(b–e)), indicating a gradual weakening of the effective stress variation.

The same incident wave induces different seabed responses for various slopes. Fig. 10 gives the FLVEL around the structure buried in different slopes undertaken the same incident wave. It is found that the FLVEL magnitude increases with increasing the slope angle α, which can be attributed to the shallower local water depth for steeper slopes. Therefore, it can be predicted that for steeper slopes, the variation of the effective stress becomes greater.

The FLVEL distribution considering different burial ratios is also shown in Fig. 11. The aforementioned disturbance only exists within a certain area around the structure. The FLVEL magnitude on the both sides of the structure gets smaller with increasing the burial ratio. The effective stress variation caused by the pore fluid flow should also become smaller.

The normalized peak uplift resistance $F_p/\gamma' H_c D$ against the local wave steepness H_p/L_p (corresponding to the burial location) for different burial ratios H_c/D and slope angles α is plotted in Fig. 12. The normalized peak uplift resistances for different burial ratios considered in the conventional design, i.e., cases of level seabed and without waves, are also presented as chain-dotted horizontal lines. It is found that the wave weakens the traditional peak uplift resistance, and the reduction in this resistance increases almost linearly as the local wave becomes steeper, for a given burial ratio H_c/D and slope angle α. This should be ascribed to the linear increase of the hydrodynamic pressure on the seabed surface with increasing the wave height. While for the same burial ratio H_c/D, the steeper the slope is, the more remarkable the reduction in the peak resistance is. Actually, two coexisting factors induce this reduction: the slope effect and wave effect. The former, though much weaker than the latter, has been discussed in the Section 4.1. For the latter, as predicted from Fig. 10, steeper slopes naturally leads to grater variation of

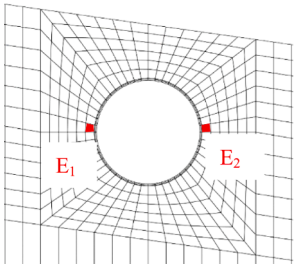

(a) Elements E_1 and E_2

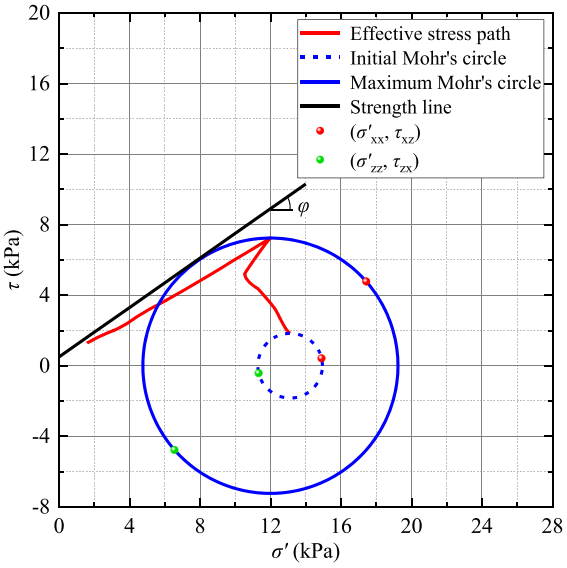

(b) α=0°, element E_1

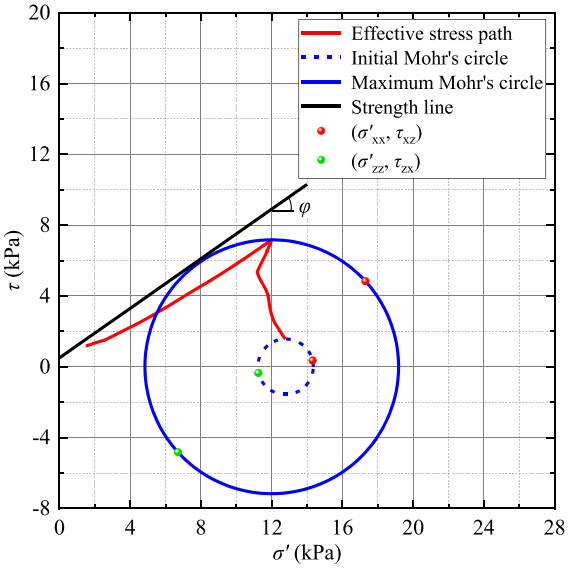

(c) α=8°, element E_1

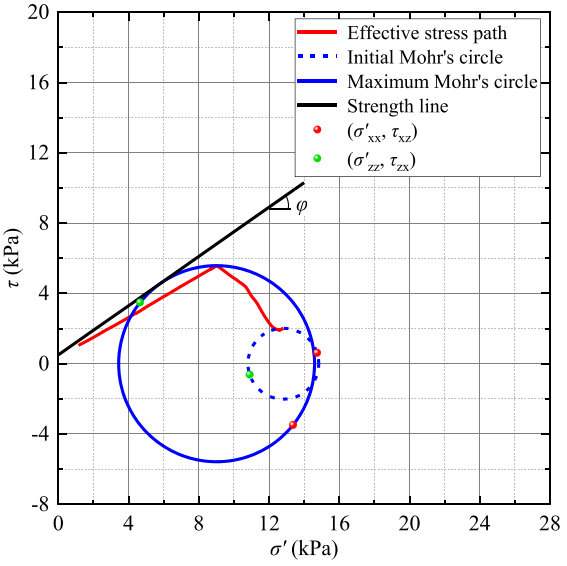

(d) α=8°, element E_2

Fig. 8. (a) Elements E_1 and E_2 and (b–d) effective stress path, initial and maximum Mohr's circle, and strength line for the centroid of these two elements at α = 0° and 8° (H_c/D = 1.0).

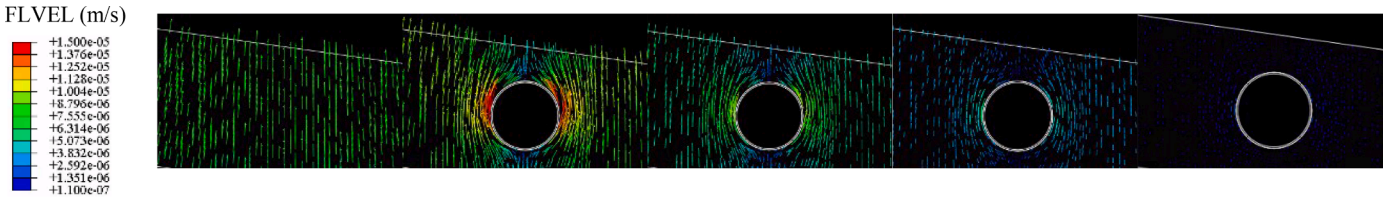

(a) Without structure H_i=9.5 m (b) H_i=9.5 m (c) H_i=6.5 m (d) H_i=3.5 m (e) H_i=1.0 m

Fig. 9. Pore fluid velocity (a) for pure seabed without structure and (b~e) around the structure undertaken waves of different incident heights (α = 8°, d_i = 33.0 m, T = 7.0 s, H_c/D = 1.0).

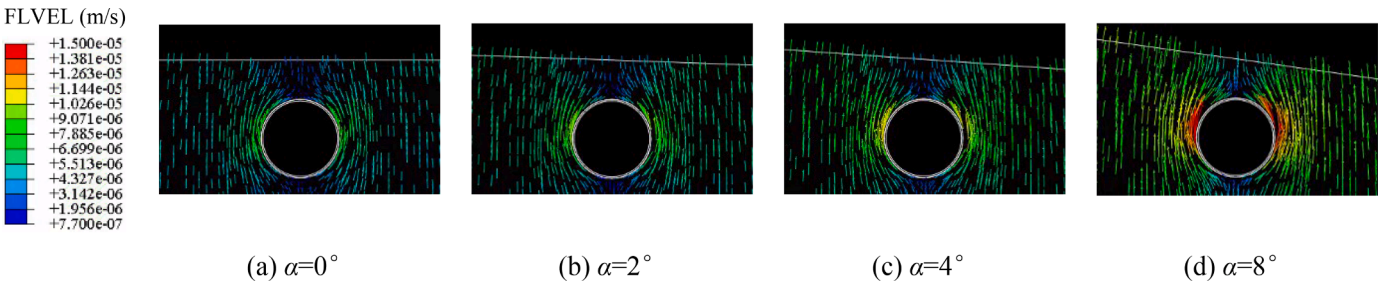

Fig. 10. Pore fluid velocity around the structure buried in different slopes (d_i = 33.0 m, T = 7.0 s, H_i = 9.5 m, H_c/D = 1.0).

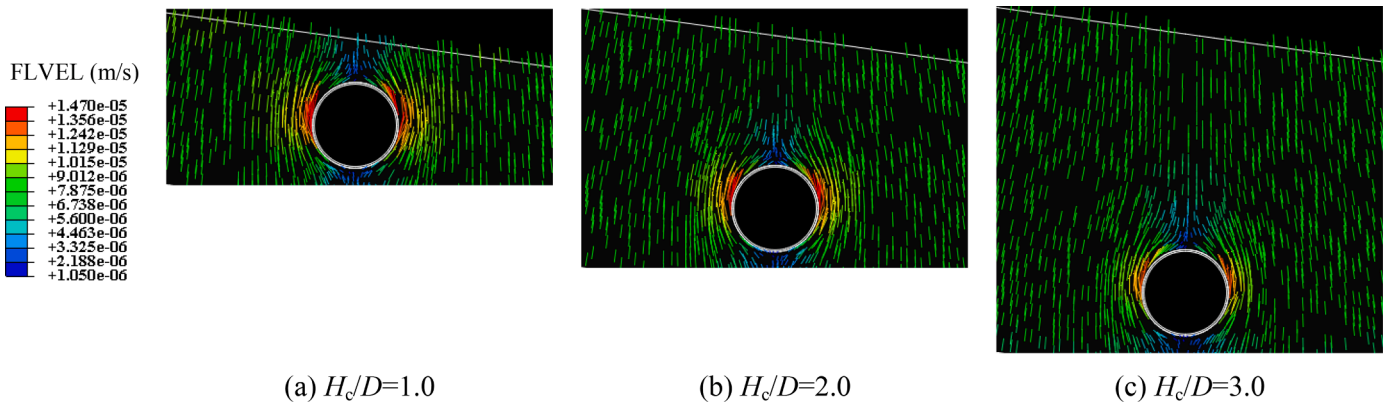

Fig. 11. Pore fluid velocity around the structure buried at different depths (α = 8°, d_i = 33.0 m, T = 7.0 s, H_i = 9.5 m).

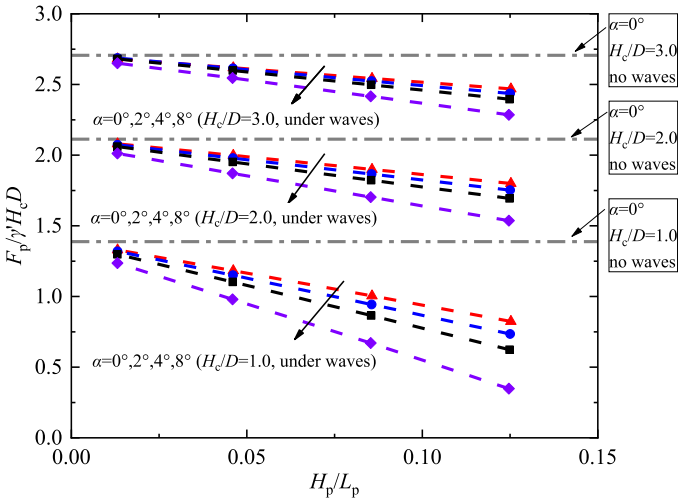

Fig. 12. Normalized peak uplift resistance against local wave steepness (d_i = 33.0 m, T = 7.0 s).

effective stress and thus larger reduction in the peak uplift resistance. Besides, the reduction progressively becomes smaller with increasing the burial ratio for a specific slope angle α (This phenomenon can also be found later in Figs. 16 and 18). This is in agreement with the finding from Fig. 11 that the change in effective stress should get smaller when increasing the burial ratio H_c/D.

Fig. 13 presents the shear bands at the peak uplift resistance for different incident wave heights. As the incident wave height increases, it can be noticed that the directions of the shear bands are almost identical to the case of no waves. However, the shear bands get wider and longer, especially the one near the slope toe. Moreover, the plastic zone appearing at the lower left side of the structure disappears when the incident wave height $H_i \geq 3.5$ m. Besides, there are two separated plastic zones emerging between the two main shear bands at H_i = 9.5 m. All these observations indicate that as the applied wave load increases, more surrounding soil near the slope toe reaches yielding state when uplift.

The effective stress path (for the uplift process only), the initial Mohr's circle (before the wave load), the Mohr's circle under the wave trough, the maximum Mohr's circle and the strength line for the centroid of the element E_1 and E_2 at the slope angle $\alpha = 8°$ are plotted in Fig. 14(a)

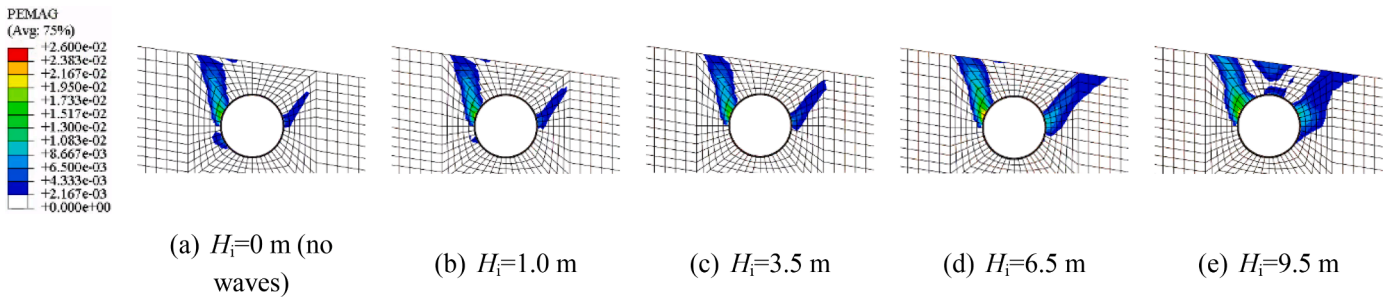

Fig. 13. Plastic strain contour at the peak uplift resistance for different incident wave heights (α = 8°, d_i = 33.0 m, T = 7.0 s, H_c/D = 1.0).

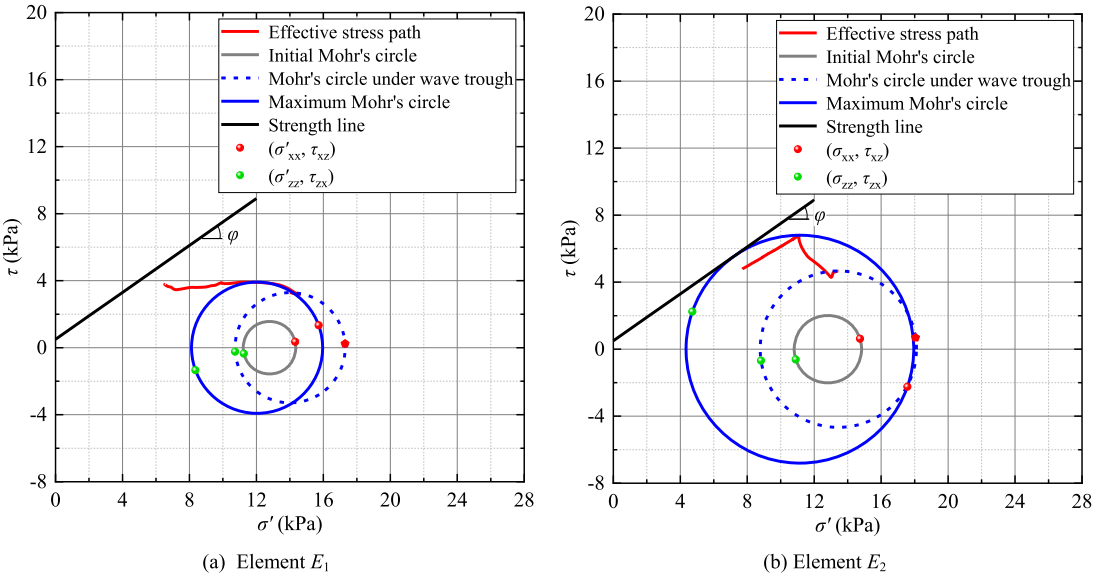

Fig. 14. Effective stress path, initial Mohr's circle, Mohr's circle under wave trough, maximum Mohr's circle and strength line for the centroid of (a) element E_1 and (b) E_2 at $\alpha = 8°$ ($d_i = 33.0$ m, $T = 7.0$ s, $H_c/D = 1.0$).

and (b), respectively, with the effective stress components (σ'_{xx}, τ_{xz}) and (σ'_{zz}, τ_{zx}) of these points marked. It is observed that the wave trough induces an increase in the horizontal effective stress σ'_{xx} and a decrease in the vertical effective stress σ'_{zz}, while the shear stress τ_{xz} (=-τ_{zx}) remains almost constant. This could be related to the direction of FLVEL shown in Figs. 9–11: upwards and towards the structure center at these two points. When uplifting the structure from the wave-induced steady state, for the element E_1, the horizontal effective stress σ'_{xx} decreases instead of increasing as in the case of no waves (see Fig. 8(c)), and its increase and decrease in shear stress τ_{xz} and vertical effective stress σ'_{zz}, respectively, are significantly smaller than those in Fig. 8(c). As a result, this point does not yield this time. For the element E_2 during uplift, the variation of effective stress components are generally similar to those occur in the case of no waves (see Fig. 8(d)). The most obvious difference lies in the decrease of vertical effective stress σ'_{zz}, which is significantly smaller than that in Fig. 8(d). And the expansion of the Mohr's circle to its maximum, i.e., the yield state in this case, is smaller compared with that in Fig. 8(d). It can be concluded again that the applied wave trough has made the surrounding soil near the slope toe more susceptible to yield.

4.2.2. *Effect of water depth*

The effect of water depth, one significant parameter influence the hydrodynamic pressure on the seabed surface (see Eq. (5)), on the aforementioned reduction is investigated in this section. Fig. 15 gives the FLVEL distribution around the structure undertaken waves of different incident water depths. It should be noted that for these different incident wave parameters, the local wave heights calculated according to Eqs. (1)–(4) do not vary much with a standard deviation of 0.057 m. Therefore, there is considerable confidence that the difference among Fig. 15(a–d) are due to the variation of incident/local water depths. In Fig. 15, it can be seen that the deeper the incident water depth, the smaller the FLVEL magnitude around the structure, implying the weaker change in the effective stress. Consequently, as expected, the normalized peak uplift resistance $F_p/\gamma' H_c D$ plotted in Fig. 16 gradually recovers as the local relative water depth d_p/L_p increases for the specific

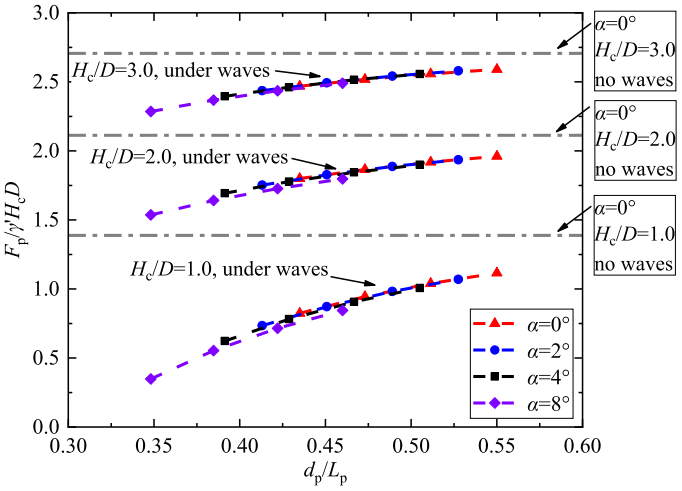

Fig. 16. Normalized peak uplift resistance against local relative water depth ($T = 7.0$ s, $H_i = 9.5$ m, $H_c/D = 1.0$).

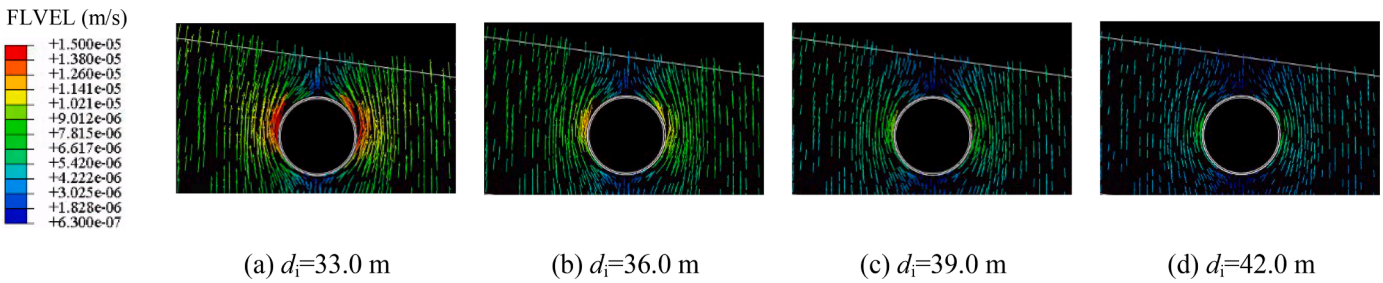

Fig. 15. Pore fluid velocity around the structure undertaken waves of different incident water depths ($\alpha = 8°$, $T = 7.0$ s, $H_i = 9.5$ m, $H_c/D = 1.0$).

burial ratio H_c/D and slope angle α. Note that for the same local relative water depth, only slight difference in the normalized resistances among different slopes is observed. It can be speculated that once the local wave parameters, i.e., local water depth, local wave height and wave period, are determined, there is only slope effect causing the resistance difference, implying the significance of the local wave parameters.

4.2.3. Effect of wave period

Usually, the larger the wave period is, the longer the wave length is, which leads to larger hydrodynamic pressure on the seabed surface (see Eq. (5)). As a result, the FLVEL magnitude shown in Fig. 17 increases as the wave period increases, implying that the variation of effective stress is enhanced at larger wave periods. Again, it is confident enough to assume that the difference among Fig. 17(a–d) are due to the wave period variation, since the standard deviation of local wave heights is only 0.039 m in the cases of these plots. Fig. 18 indeed indicates that the normalized peak uplift resistance $F_p/\gamma' H_c D$ decreases gradually with increasing the wave period T for the specific burial ratio H_c/D and slope angle α. As for the burial ratio and slope angle, similar effects have been discussed in Fig. 12 and will not be repeated here for brevity.

4.3. Prediction for the uplift resistance reduction

Previous numerical results indicate that both the slope effect and wave effect reduce the peak uplift resistance of the structure shallowly buried in slopes undertaken the wave load. This section attempts to quantify this reduction R, which consists of the reduction from the slope effect R_s, and that from the wave effect R_w. And R is defined from the following expression:

$$f_{s,w} = (1-R) f_{s0,w0} = [1-(R_s + R_w)] f_{s0,w0} \tag{12}$$

where $f_{s,w}$ is the normalized peak uplift resistance $F_p/\gamma' H_c D$ considering both the slope effect and wave effect, while $f_{s0,w0}$ is the conventional normalized resistance $F_p/\gamma' H_c D$, i.e., for the level seabed and without wave actions. In this study, R_s is directly calculated from the results in the Section 4.1, and R_w can be determined as R- R_s, in which R is obtained from the results in the Section 4.2.

The reduction from the slope effect R_s versus the slope angle α is plotted in Fig. 19(a) for different burial ratios H_c/D, and corresponding relation between R_s, α and H_c/D is fitted as:

$$R_s = 4.38\alpha^2 \cdot e^{-0.81\frac{H_c}{D}} \tag{13}$$

Note that the slope angle α in this equation should be radian number. Generally speaking, these curves are in good agreement with the numerical results, especially for those cases of small burial ratio. The growth of R_s is well reflected with increasing α or decreasing H_c/D, respectively.

Qi et al. (2020) gave the following empirical expression to describe the wave effect:

$$R_w = 0.82 \frac{p_w}{\gamma' H_c} (H_c/D = 1.0, D = 1.0 \text{ m}) \tag{14}$$

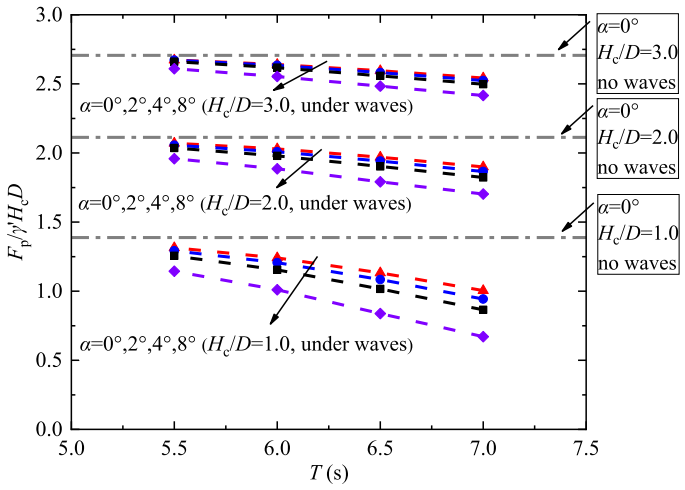

Fig. 18. Normalized peak uplift resistance against wave period (d_i = 33.0 m, H_i = 6.5 m, H_c/D = 1.0).

However, in their 16 numerical cases, the burial ratio H_c/D and the pipeline outer diameter D are constant, so that the extrapolation of Eq. (14) to other burial ratios is questionable. For instance, Fig. 20 gives the numerical results of this study (H_c/D = 1.0, 1.5 and 2.0) and the prediction of Eq. (14). It is obvious that Eq. (14) is not a good predictor for the cases of $H_c/D \neq 1.0$. Therefore, a new predictive formula is proposed in this study to cover larger burial ratios. The opposite normalized vertical average gradient of the excess pore pressure at the depth H_c with respect to that at the seabed surface, j'_c, is defined to quantify the wave effect for a specific burial ratio H_c/D:

$$j'_c = -\frac{p_c - p_w}{(-H_c - 0)\gamma_w} \tag{15}$$

in which p_c is the wave-induced excess pore pressure at the depth H_c, using the solution in Madsen (1978), Eq. (9c), as a first-order approximation, thus,

$$j'_c = \frac{(e^{kH_c} - 1) p_w}{\gamma_w H_c} \tag{16}$$

Fig. 19(b) gives the numerical results of R_w for different j'_c and H_c/D as well as the fitted curves. R_w can be expressed as:

$$R_w = 22.81 j'_c \cdot e^{-0.88\frac{H_c}{D}} \tag{17}$$

Similar to Fig. 19(a), although there is a slight deviation at H_c/D = 3.0, which might result from the diminished slope effect and wave effect, and ensuing less accuracy, an good agreement between the numerical results and the fitted ones can be observed overall. The growth of R_w is well reflected with increasing j'_c or decreasing H_c/D, respectively.

In Fig. 21(a), the experimental results in Huang et al. (2021a), which is discussed in Fig. 5, are compared with the prediction Eq. (13). It is found that the overall trend is acceptable, but there are still some

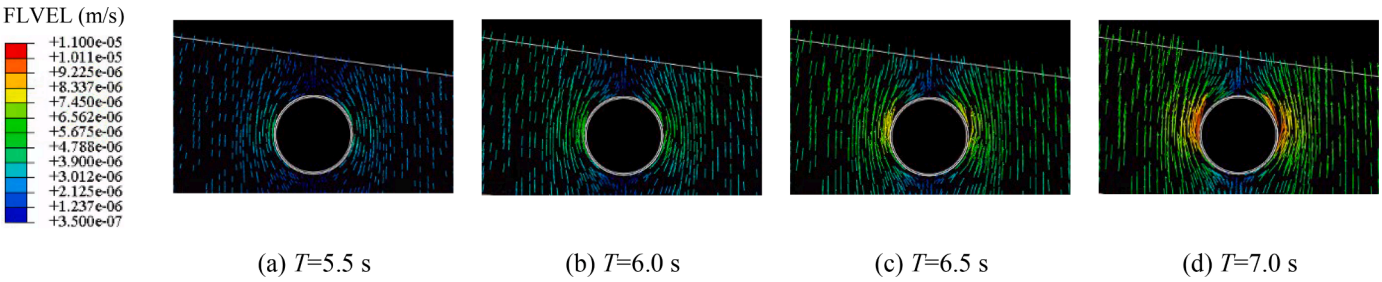

Fig. 17. Pore fluid velocity around the structure undertaken waves of different periods (α = 8°, d_i = 33.0 m, H_i = 6.5 m, H_c/D = 1.0).

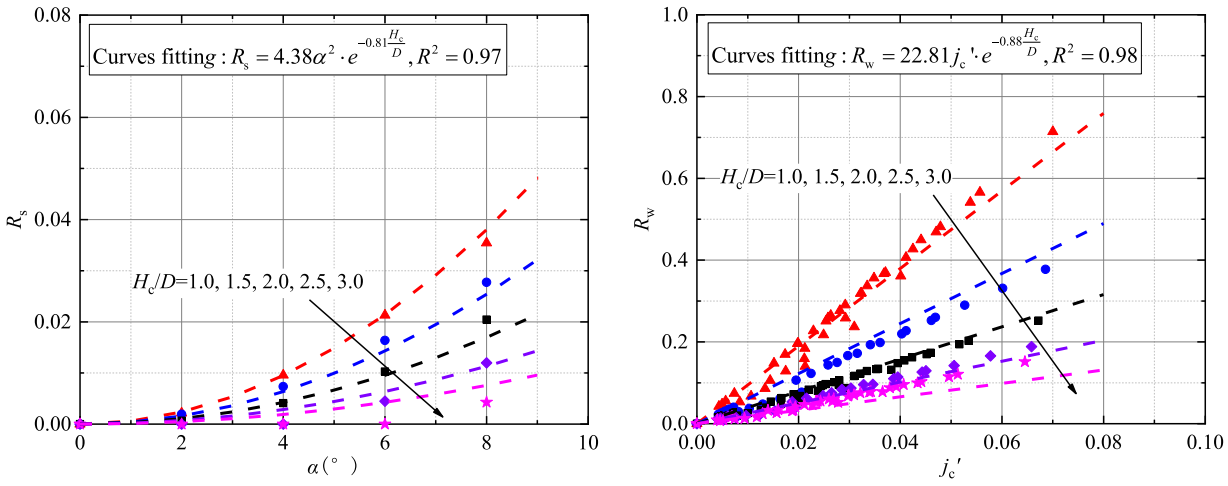

(a) Slope effect (b) Wave effect

Fig. 19. Reduction formulation from the numerical results considering (a) slope effect and (b) wave effect.

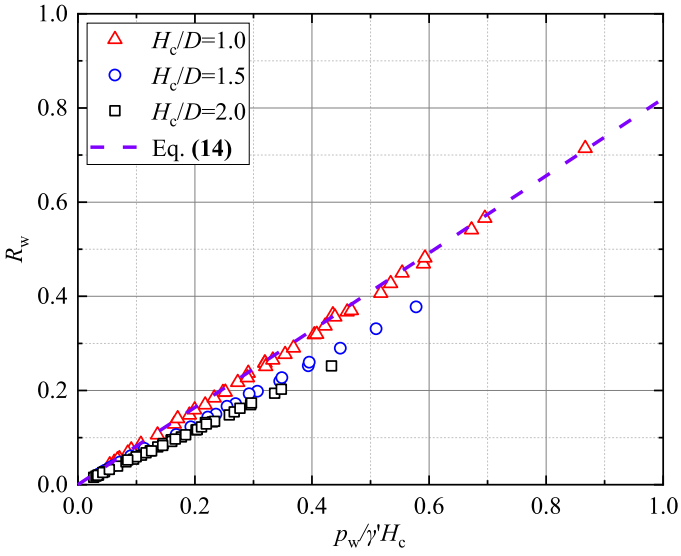

Fig. 20. The applicability of Eq. (14) to this study.

deviations in the R_s values. This might be attributed to that (1) the formula Eq. (13) is fitted from the cases of $\alpha \leq 8°$; and (2) the soil properties have not been taken into account in Eq. (13). And this might imply the exact applicability of Eq. (13) in $\alpha \leq 8°$ and medium dense sand. Numerical results from Qi et al. (2020), whose parameters are

Table 5
Parameters used in the numerical model in Qi et al. (2020).*

Wave parameters	
Water depth d (m)	12.0 (various)
Wave height H (m)	7.0 (various)
Wave period T (s)	2.0 (various)
Seabed parameters	
Effect unit weight γ'(kN/m^3)	7.84
Young's modulus E_s (kPa)	50,000
Poisson's ratio ν_s	0.3
Friction angle φ (°)	30
Pipeline parameters	
Outer diameter D (m)	1.0
Wall thickness t_w (mm)	20
Young's modulus E_p (GPa)	210
Poisson's ratio ν_p	0.19
Interface friction coefficient μ	0.3

* Note that $H_c/D = 1.0$ and the pipeline is weightless in this study.

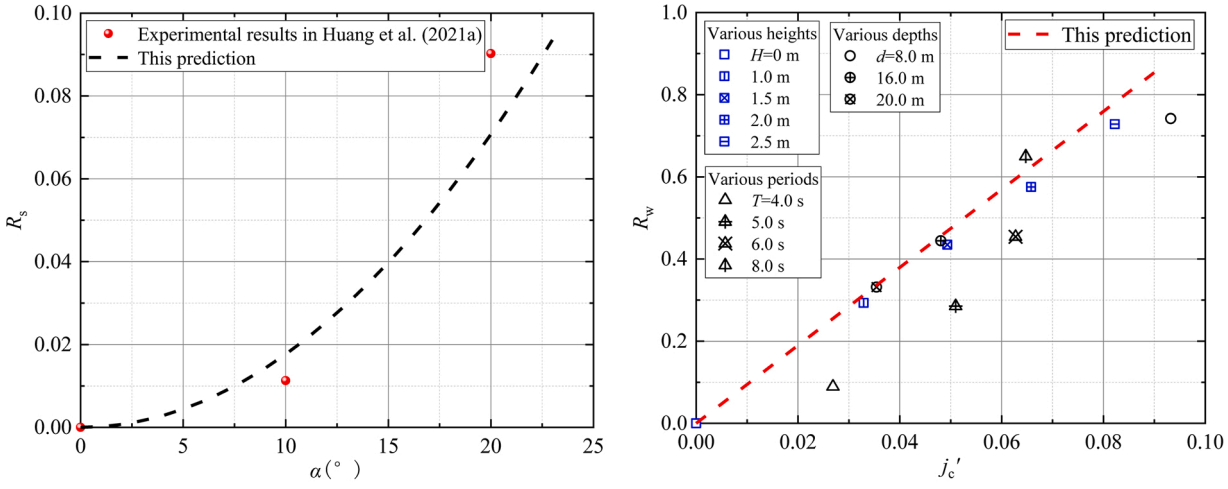

(a) Slope effect (b) Wave effect

Fig. 21. Comparison between the predictive formulae and available experimental/numerical results.

summarized in Table 5, are used to verify the predictive formulas Eq. (17) in Fig. 21(b). Notice that considerable agreement between the two results is reached, except for the cases of short wave length L (less than 55 m here). This indicates that the solution in Madsen (1978), which originally aimed at the wave-induced seabed response without structure, might not be accurate enough to be used in Eq. (16) when the ratio $D/L \geq 0.018$.

5. Conclusion

The current practice for the pipe-soil interaction mainly focuses on the pipelines buried in the level ground and not subjected to the wave load. For the offshore slender structures shallowly buried in slopes and undertaken wave actions, this study numerically investigated their peak uplift resistances. Multiple factors, i.e., the slope effect and wave effect, were taken into account simultaneously. The main conclusions can be drawn as follows:

(1) The normalized peak uplift resistance $F_p/\gamma' H_c D$ decreases as the slope angle α increases, especially for smaller burial ratios H_c/D. Compared with the level seabed, the two main shear bands have a little rotation towards the slope toe when uplifting the buried structure. More surrounding soil near the slope crest yields, while less surrounding soil near the slope toe yields. The slope effect produces asymmetric stress state variation of the soil on both sides of the structure when it is uplifted, and the reduction in the peak resistance may be caused by the lower strength mobilization of the surrounding soil near the slope toe.
(2) After the wave load applied, the FLVEL field surrounding the structure is not as homogenous as that in the pure seabed. And its magnitude around the structure grows with increasing the incident wave height, increasing the slope angle or decreasing the burial ratio. The variation of effective stress will be strengthened by this growth.
(3) The peak uplift resistance reduces after the wave load applied, and the reduction grows almost linearly with the local wave steepness for the given burial ratio H_c/D and slope angle α. While for the same burial ratio H_c/D, the steeper the slope is, the more remarkable the reduction is. Besides, the reduction progressively becomes smaller with increasing the burial ratio for a specific slope angle α. As the incident wave height increases, more surrounding soil near the slope toe reaches the yielding state when uplift.
(4) For the specific burial ratio H_c/D and slope angle α, the normalized peak uplift resistance $F_p/\gamma' H_c D$ gradually recovers as the local relative water depth d_p/L_p increases, while it reduces with increasing the wave period T. These phenomena are also linked to the variation of the FLVEL field around the structure.
(5) Based on the numerical results, a preliminary predictive formula for the previous reduction R is proposed and compared with the available experimental/numerical results.

For the peak uplift resistance investigated in this study, only the linear wave-induced seabed response was considered, so it should only be applicable to submarine mild slopes or quiet bays that are not affected by highly nonlinear waves such as typhoon-induced storms. Further studies should simulate nonlinear waves and breaking waves that are widely present in the offshore environment. Perhaps a numerical solution with CFD software like openFOAM could be used to solve this problem. Furthermore, it has to be mentioned that the effect of scour due to the drastic hydrodynamics was neglected, and the focus of this study was the peak uplift resistance before the scour occurred or after the equilibrium was reached. As for the process of seabed scour, accompanied with the time-varying thickness of the cover layer of buried structures, was not accounted for in this preliminary study. This implies that the mechanics of sediment movement should be incorporated into the further investigation.

CRediT authorship contribution statement

Hongkuan Yang: Data curation, Writing – original draft. **Zhen Guo:** Conceptualization, Investigation, Supervision, Software, Writing – review & editing. **Lizhong Wang:** Project administration, Writing – review & editing. **Wengang Qi:** Software, Writing – review & editing.

Declaration of Competing Interest

The authors declared that they have no conflicts of interest to this work.

We declare that we do not have any commercial or associative interest that represents a conflict of interest in connection with the work submitted.

Acknowledgments

The authors would like to acknowledge the supports from Finance Science and Technology Project of Hainan Province (ZDKJ202019), Major Science and Technology Project of Sanya (No. SKJC-2020-01-016), and Natural Science Foundation of Zhejiang Province (LR22E080005).

References

Abduljauwad, S.N., Al-Ghamedy, H.N., Siddiqui, J.A., Asi, I.M., Al-Shayea, N.A., 2004. Stability of vertically bent pipelines buried in sand. J. Press. Vessel Technol. 126 (3), 382–390.
ALA, 2005. Guidelines for the Design of Buried Steel Pipe. Federal Emergency Management Agency (FEMA) and American Society of Civil Engineers (ASCE), Washington, DC and Reston, VA, USA.
Bonjean, D., Erbrich, C., Zhang, J., 2008. Pipeline flotation in liquefiable soil. In: Proceedings of the Offshore Technology Conference. OTC, p. 19668.
Carter, L., Burnett, D., Drew, S., Marle, G., Hagadorn, L., Bartlett-McNeil, D., Irvine, N., 2009. Submarine Cables and the Oceans: Connecting the World. ICPC/UNEP/UNEP-WCMC. UNEP-WCMC Biodiversity Series No. 31.
Chaloulos, Y.K., Bouckovalas, G.D., Zervos, S.D., Zampas, A.L., 2015. Lateral soil–pipeline interaction in sand backfill: effect of trench dimensions. Comput. Geotech. 69, 442–451.
Chen, R., Wu, L., Zhu, B., Kong, D., 2019. Numerical modelling of pipe-soil interaction for marine pipelines in sandy seabed subjected to wave loadings. Appl. Ocean Res. 88, 233–245.
Cheng, A.H.D., Liu, P.L.F., 1986. Seepage force on a pipeline buried in a poroelastic seabed under wave loadings. Appl. Ocean Res. 8 (1), 22–32.
Damgaard, J.S., Sumer, B.M., Teh, T.C., Palmer, A.C., Foray, P., Osorio, D., 2006. Guidelines for pipeline on-bottom stability on liquefied noncohesive seabeds. J. Waterw. Port Coast. Ocean Eng. 132 (4), 300–309. ASCE.
Det Norske Veritas (DNV), 2007. Global Buckling of Submarine Pipelines Structural Design Due To High Temperature/High Pressure. DNV-RP-F110. 1–64.
Det Norske Veritas (DNV), 2017. Pipe-soil interaction for submarine pipelines DNVGL-RP-F114, 1–96.
Dunn, S.L., Vun, P.L., Chan, A.H.C., Damgaard, J.S., 2006. Numerical modeling of wave-induced liquefaction around pipelines. J. Waterw. Port Coast. Ocean Eng. 132 (4), 276–288.
Gao, F.P., Han, X.T., Cao, J., Sha, Y., Cui, J.S., 2012. Submarine pipeline lateral instability on a sloping sandy seabed. Ocean Eng. 50, 44–52.
Gao, F.P., Wang, N., Li, J., Han, X.T., 2016. Pipe–soil interaction model for current-induced pipeline instability on a sloping sandy seabed. Can. Geotech. J. 53, 1822–1830.
Gatmiri, B., 1990. A simplified finite element analysis of wave-induced effective stresses and pore pressures in permeable sea beds. Géotechnique 40 (1), 15–30.
Haigh, S.K., 2021. Flotation of pipes and cables in consolidating backfill. Géotechnique 71 (4), 299–304.
Herbich, J.B., Schiller, R.E., Dunlap, W.A., Watanabe, R.K., 1984. Seafloor Scour—Design Guidelines for Ocean-Founded Structures. Marcel Dekker Incorporated, New York.
Hsu, C.J., Tsai, C.C., Chen, Y.Y., 2021. Wave-induced seabed momentary liquefaction in shallow water. Appl. Ocean Res. 115, 102819.
Hsu, J.R.C., Jeng, D.S., 1994. Wave-induced soil response in an unsaturated anisotropic seabed of finite thickness. Int. J. Numer. Anal. Methods Geomech. 18, 785–807.
Huang, B., Liu, J, Fan, J, Ling, D, 2021b. Analytical solution for upheaval buckling of shallow buried pipelines in inclined cohesionless soil. J. Zhejiang Univ. Sci. A 22 (5), 369–381.
Huang, B., Liu, J., Fan, J., Ling, D., 2021a. Experimental study on uplift mechanisms of pipes buried in sloping medium dense sand. J. Pipeline Syst. Eng. Pract. 12 (3), 04021027. ASCE.

Ismail, S., Sadek, S., Najjar, S.S., Mabsout, M., 2021. Numerical finite element modelling of soil resistance against upheaval buckling of buried submarine pipelines. Appl. Ocean Res. 106, 102478.
Jeng, D.S., Zhao, H.Y., 2015. Two-dimensional model for accumulation of pore pressure in marine sediments. J. Waterw. Port Coast. Ocean Eng. 141 (3), 04014042.
Jung, J.K., O'Rourke, T.D., Olson, N.A., 2013. Uplift soil–pipe interaction in granular soil. Can. Geotech. J. 50, 744–753.
Katebi, M., Wijewickreme, D., Maghoul, P., Roy, K., 2021. Lateral force–displacement response of buried pipes in slopes. Géotechnique. https://doi.org/10.1680/jgeot.21.00057.
Kouretzis, G.P., Sheng, D., Sloan, S.W., 2013. Sand–pipeline–trench lateral interaction effects for shallow buried pipelines. Comput. Geotech. 54, 53–59.
Liang, Z., Jeng, D.S., Liu, J., 2020. Combined wave–current induced seabed liquefaction around buried pipelines: design of a trench layer. Ocean Eng. 212, 107764.
Madsen, O.S., 1978. Wave-induced pore pressures and effective stresses in a porous bed. Géotechnique 28 (4), 377–393.
Magda, W., Maeno, S., Nago, H., 2000a. Floatation of buried submarine pipeline under cyclic loading of water pressure-numerical and experimental studies. J. Fac. Environ. Sci. Technol. Okayama Univ. 5 (1), 81–98.
Magda, W., Maeno, S., Nago, H., 2000b. Floatation of buried submarine pipeline under cyclic loading of water pressure-numerical and experimental studies. J. Fac. Environ. Sci. Technol. Okayama Univ. 5 (1), 81–98.
Miche, M., 1944. Mouvements ondulatoires de la mer en profondeur constante ou décroissante. Ann. Ponts Chaussées. http://resolver.tudelft.nl/uuid:6fceef55-d71b-4e3e-a94f-98ff17cb8f91.
Miyamoto, J., Sassa, S., Sekiguchi, H., 2004. Progressive solidification of a liquefied sand layer during continued wave loading. Géotechnique 54 (10), 617–629.
Miyamoto, J., Sassa, S., Tsurugasaki, K., Sumida, H., 2020. Wave-induced liquefaction and floatation of a pipeline in a drum centrifuge. J. Waterw. Port Coast. Ocean Eng. 146 (2), 04019039.
Neelamani, S., Al-Banaa, K., 2012. Variation in wave forces on buried submarine pipeline in different types of soils in random waves. In: Proceedings of the 31st International Conference on Ocean, Offshore and Arctic Engineering. ASME.
Qi, W.G., Shi, Y.M., Gao, F.P., 2020. Uplift soil resistance to a shallowly-buried pipeline in the sandy seabed under waves: poro-elastoplastic modeling. Appl. Ocean Res. 95, 102204.
Rafiei, A., Rahman, M.S., Gabr, M.A., 2019. Coupled analysis for response and instability of sloping seabed under wave action. Appl. Ocean Res. 88, 99–110.
Robert, D.J., Thusyanthan, N.I., 2018. Uplift resistance of buried pipelines in partially saturated sands. Comput. Geotech. 97, 7–19.
Roopsekhar, K.A., Sundar, V., 2004. Regular wave pressures and forces on submerged pipelines near a sloping boundary. Ocean Eng. 31, 2295–2317.
Roy, K., Hawlader, B., Kenny, S., Moore, I., 2018a. Uplift failure mechanisms of pipes buried in dense sand. Int. J. Geomech. 18 (8), 04018087. ASCE.
Roy, K., Hawlader, B., Kenny, S., Moore, I., 2018b. Upward pipe–soil interaction for shallowly buried pipelines in dense sand. J. Geotech. Geoenviron. Eng. 144 (11), 04018078. ASCE.
Roy, K.S., 2012. Finite Element Analyses of Soil/Pipeline Interactions in Sand with an Advanced Soil Constitutive model. Memorial University of Newfoundland. Master's Thesis.
Sassa, S., Sekiguchi, H., 1999. Wave-induced liquefaction of beds of sand in a centrifuge. Géotechnique 49 (5), 621–638.
Sassa, S., Sekiguchi, H., 2001. Analysis of wave-induced liquefaction of sand beds. Géotechnique 51 (2), 115–126.
Sudhan, C.M., Sundar, V., Rao, S.N., 2002. Wave-induced forces around buried pipelines. Ocean Eng. 29, 533–544.
Sumer, B.M., Fredsøe, J., Christensen, S., Lind, M.T., 1999. Sinking/floatation of pipelines and other objects in liquefied soil under waves. Coast. Eng. 38, 53–90.
Sumer, B.M., Hatipoglu, F., Fredsøe, J., Hansen, N.E.O., 2006a. Critical flotation density of pipelines in soils liquefied by waves and density of liquefied soils. J. Waterw. Port Coast. Ocean Eng. 132, 252–265.
Teh, T.C., Palmer, A.C., Damgaard, J.S., 2003. Experimental study of marine pipelines on unstable and liquefied seabed. Coast. Eng. 50, 1–17.
Trautmann, C.H., O'Rourke, T.D., Kulhawy, F.H., 1985. Uplift force-displacement response of buried pipe. J. Geotech. Eng. 111 (9), 1061–1076. ASCE.
Ülker, M.B.C., 2021. A combined theoretical and numerical modeling study of cyclic nonlinear response of sandy seabed. Ocean Eng. 219, 108348.
Ulker, M.B.C., Rahman, M.S., Jeng, D.S., 2009. Wave-induced response of seabed: various formulations and their applicability. Appl. Ocean Res. 31, 12–24.
Weggel, J.R., 1972. Maximum breaker height. J. Waterw. Harb. Coast. Div. 98 (ww4), 529–548. ASCE.
White, D.J., Barefoot, A.J., Bolton, M.D., 2011. Centrifuge modelling of upheaval buckling in sand. Int. J. Phys. Model. Geotech. 2, 19–28.
White, D.J., Cheuk, C.Y., Bolton, M.D., 2008. The uplift resistance of pipes and plate anchors buried in sand. Géotechnique 58 (10), 771–779.
Ye, J.H., Jeng, D.S., 2012. Response of porous seabed to nature loadings: waves and currents. J. Eng. Mech. 138 (6), 601–613. ASCE.
Zen, K., Yamazaki, H., 1990. Mechanics of wave-induced liquefaction and densification in seabed. Soils Found. 30 (4), 90–104.
Zen, K., Yamazaki, H., 1991. Field observation and analysis of wave-induced liquefaction in seabed. Soils Found. 31 (4), 161–179.